Effect of wettability and textile architecture on fluid displacement and pore formation during infiltration of carbon fibrous preforms

Teixidó, Helena; Caglar, Baris; Michaud, Véronique

DOI
10.1016/j.compositesa.2023.107733

Publication date
2023

Document Version
Final published version

Published in
Composites Part A: Applied Science and Manufacturing

Citation (APA)
Teixidó, H., Caglar, B., & Michaud, V. (2023). Effect of wettability and textile architecture on fluid displacement and pore formation during infiltration of carbon fibrous preforms. *Composites Part A: Applied Science and Manufacturing*, *174*, Article 107733. https://doi.org/10.1016/j.compositesa.2023.107733

Composites: Part A 174 (2023) 107733

Contents lists available at ScienceDirect

Composites Part A

journal homepage: www.elsevier.com/locate/compositesa

Effect of wettability and textile architecture on fluid displacement and pore formation during infiltration of carbon fibrous preforms

Helena Teixidó [a], Baris Caglar [b], Véronique Michaud [a,*]

[a] Laboratory for Processing of Advanced Composites (LPAC), Institute of Materials (IMX), Ecole Polytechnique Fédérale de Lausanne (EPFL), Station 12, 1015 Lausanne, Switzerland
[b] Aerospace Structures and Materials Department, Faculty of Aerospace Engineering, Delft University of Technology, Kluyverweg 1, Delft 2629HS, Netherlands

ARTICLE INFO

Keywords:
A. Carbon Fibers
B. Porosity
B. Wettability
E. Resin Flow

ABSTRACT

We seek to address how air entrapment mechanisms during infiltration are influenced by the wetting characteristics of the fluid and the pore network formed by the reinforcement. To this end, we evaluated the behavior of two model fluids with different surface tensions, infiltrating three carbon fiber reinforcements, by means of X-ray radiography. We also assessed initial (dry) and final (wetted) states for each experiment by performing X-ray CT scans. We found that the fluid characteristics strongly affect the flow front patterns and pore filling events for a given fabric architecture. Two main promoters of snap-off events are involved in capillary dominated flows: a very wetting system leading to corner flows and the fabric bundles oriented perpendicular to the flow acting as obstacles, specifically in fabric architectures prone to variations in nesting. Finally, we evaluated the applicability of a pore network model to further link preform architecture and void formation.

1. Introduction

Liquid composite molding (LCM) processes belong to infiltration processes, in which the resin movement inside the open pore space of a dry fibrous preform can be described as displacement of two immiscible fluids inside a porous medium, a phenomenon which is found in many natural and engineering occurrences [1]. However, despite the broad literature on this topic, a complete understanding of flow kinetics and morphology has not been reached so far due to the complex interplay of several factors such as heterogeneity of the porous network, fluid properties (viscosity, density, and surface tension), wettability, flow displacement speeds, void formation, and transport mechanisms as well as the considered length scales [2]. Concretely, fluid transport can be described at the scale of a pore (micro-scale) in which parameters such as pore connectivity, roughness, and fluid/solid interfacial properties govern the fluid movement or at the meso- or Darcy-scale in which the flow is defined by a continuum mechanics approach in a representative volume element characterized by the medium porosity, permeability and saturation. The relationship between the physical phenomena taking place in these two scales remains unclear particularly because the pore-scale spatial heterogeneity highly affects the flow at the macro-scale [3,4]. Inevitably, during infiltration, an unstable displacement of the invading fluid takes place and flow generates preferential pathways, resulting in a non-uniform flow progression within regions sometimes causing entrapment of the displaced fluid. In LCM, air entrapment arising from an inefficient filling has proved to be the most common flow-induced defect detrimentally affecting the final composite part properties [5,6].

The flow displacement morphology in a porous medium is recognized to be affected by the viscosity ratio between liquid and air and by the capillary number Ca, defined as the ratio between viscous and capillary forces [7]. Although several definitions for Ca have been proposed over the years, the preferred form is the most concise one containing the resin Darcy superficial velocity U, viscosity η, and surface tension γ, as [8]:

$$Ca = \frac{U\eta}{\gamma} \tag{1}$$

At the flow front, a constant competition between viscous and capillary forces takes place and researchers agree with the existence of an optimal capillary number Ca_{opt}, for which capillary and viscous effects compensate each other and the amount of the voids is minimal (i.e. flow velocities are comparable in inter- and intra-bundles regions) [9–13]. Since Ca_{opt} is possibly influenced by textile architecture and

* Corresponding author.
E-mail address: veronique.michaud@epfl.ch (V. Michaud).

https://doi.org/10.1016/j.compositesa.2023.107733
Received 23 March 2023; Received in revised form 4 August 2023; Accepted 6 August 2023
Available online 7 August 2023

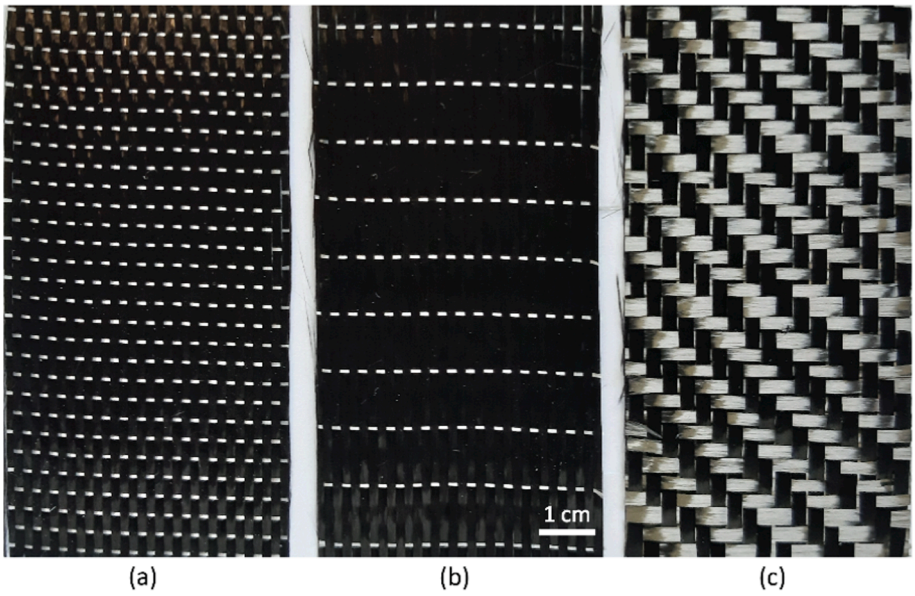

Fig. 1. (a) original unidirectional (UD), (b) modified unidirectional (UDM) and (c) twill (TW) carbon fabrics.

fluid properties, it is specific for a given resin/reinforcement system and to date, no one has been able to predict it quantitatively. Moreover, resins are usually injected into the mold at a constant pressure, resulting in a decrease of impregnation speed with time (triggering a wide range of capillary numbers) and non-homogeneous patterns [14].

Owing to the presence of high-volume fraction tows in textiles, capillary forces manifest themselves in composites processing and have proven to be responsible of an incomplete resin filling in the fibrous preform [15]. It is usual in composite processing to estimate the capillary pressure ΔP_γ acting at the flow front, by assuming a saturated flow (or slug-flow approach), and the capillary pressure drop acting as a boundary condition at the location of the flow front, written as [16]:

$$\Delta P_\gamma = -S_f \gamma \cos(\theta) \tag{3}$$

where θ is the fluid/fabric contact angle and S_f the area of fluid-fiber interface per unit volume of fluid. By influencing the pressure profile, ΔP_γ has an impact on the infiltration kinetics and Eq. (3) highlights the direct impact of dynamic wettability on capillary forces. Moreover, the dual-scale architecture of textiles with micro and meso pores respectively located in the intra- and inter-tow spaces triggers a dual-scale flow and a void entrapment mechanism [5,6]. At high impregnation speeds, it was shown that the resin tends towards a dynamic non-wetting behavior and viscous fingering takes place in *meso*-spaces, hence flow inside the tows is delayed and micro-voids remain trapped there. Conversely, at low impregnation speeds, fluid is driven by capillary wicking preferentially filling micro-spaces inside the tows, displaying an overall wetting behavior, *meso*-voids are in this case formed in between the tows. Consequently, when the fluid moves with a certain velocity, the thermodynamic equilibrium is not respected anymore and wetting becomes a dynamic property that depends on the resin-fabric system [14,17,18]. According to the physics of porous media, wettability is a pore-scale property that has a significant impact on capillarity, residual trapping, and hysteresis in porous media systems, in turn acting on the macroscopic Darcy scale [19]. Nevertheless, there is still some controversy surrounding the dynamic effect of wettability on infiltration behavior in a confined porous medium with a given spatial distribution of pores and this topic remains to this day a major scientific challenge [17,20–23].

In composites, a good wetting between matrix and fibers is sought to ensure good interfacial adhesion. Commonly, static and dynamic wetting are characterized at the microscale with single fiber measurements techniques (and extended to the *meso*-tow scale in ref. [18]) by direct optical visualization and the Wilhelmy method [24–28] and at the *meso*-tow and macro-layer scales with wicking experiments and the Washburn method [29–32]. The influence of wetting on the overall pressure driven flow kinetics has seldom been addressed in LCM. Recently, Caglar et al. [33] showed an increased dynamic wetting behavior for corona treated glass fabrics and the related change of the flow front morphology. Similarly, Yoshihara et al. [34], showed that wetting exerts a strong effect on the impregnation behavior and the void processes in a single layer of pristine and fluorine coated woven glass fabrics.

Flow studies also rely on a good description of the pore space geometry and topology. Nowadays, X-ray techniques have allowed to image and reconstruct in 3D the porosity of fibrous preforms with unprecedented spatial resolution [35–37]. An improved description of the pore-network has enabled to perform numerical models to simulate, predict and gain a better insight on flow kinetics (in LCM processes, mainly to assess the permeability). For porous media made out of soil or rocks, a pore network model (PNM) is frequently employed to simply characterize the architectural features of the porous media, such as tortuosity, connectivity, pore size distribution. The principle is to describe the available volume as a set of pores linked with throats that describe the connectivity [38,39]. Nevertheless, this approach is still seldom applied in the frame of composite systems [40–42].

In Ref [43] we modelled the displacement of a model fluid into a carbon preform by means of macroscopic saturation profiles and the two-phase flow extension of Darcy's law. However, these descriptions give very little insight on the flow regimes at the pore scale, where local capillary forces play a major role. In the present work, we investigate the effect of a change in the fluid wetting characteristics on the flow morphology, and the fluid displacement events taking place in the unsaturated area behind the flow front, for three woven carbon fabrics architectures (a twill fabric and a UD fabric with and without geometrical modifications induced by removal of transverse stitches). For this, we performed constant flow rate experiments with two fluids of different static surface tensions but similar viscosity, both containing contrasting agents, and we observed their infiltration in-situ, in 2D averaged over the thickness with X-ray radiography. We then assessed the pore network geometry by using a pore network model and carried out a void analysis stemming from capillary/viscous phenomena by performing 3D tomographic scans of the dry (before) and wet (after impregnation) preform states, in order to better elucidate the role of wetting and fiber architecture on the flow and porosity patterns.

Table 1
Fluid properties.

Fluid	Density* [g/ml]	Surface tension* [mN/m]	Viscosity* [Pa•s]	E_a[kJ•mol^{-1}]	B[Pa•s]
PEG based	1.276	32.7	0.075	−20.79	$1.715 \bullet 10^{-5}$
Glycerol based	1.400	65.5	0.074	−40.96	$4.900 \bullet 10^{-9}$

*Values at 25 °C.

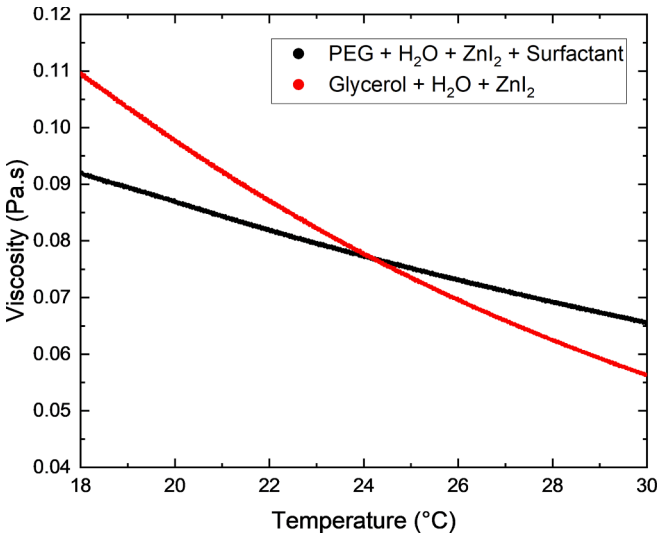

Fig. 2. Viscosity-temperature curves of infiltrating fluids.

2. Materials and methods

2.1. Materials

The quasi-unidirectional carbon fabric from Suter Kunststoffe AG (called UD) with superficial density, A_w = 270 g/m^2, previously employed in Refs. [43,44], was used (Fig. 1a). Warp tows (400 tex) contain 6000 filaments of carbon fibers and, in order to maintain the fibers together, E-glass tows (34 tex) are woven in the weft direction. The glass fibers have a bulk density of 2.60 g/cm^3 and a diameter of 9 μm. Then, the original fabric structure was modified by removing two over three horizontal glass bundles resulting in the fabric shown in Fig. 1b with the aim of making the fabric more unidirectional. The areal weight of the modified UD carbon fabric (called UDM) was estimated to 263 g/m^2. A twill carbon fabric (called TW, A_w = 285 g/m^2), presenting a higher bidirectionality, was purchased from Suter Kunststoffe AG (Fig. 1c). Warp and weft tows had a linear density of 200 tex with 3000 filaments of fibers. The carbon fibers were the same for both fabrics: Tenax HTA 3151 fibers from Teijin with density 1.76 g/cm^3 and a diameter of 7 μm according to the datasheet.

Two model fluids were employed: a water-based solution of polyethylene glycol (PEG, Sigma Aldrich, 35 kDa) and a water-based solution of glycerol (99.5%, Mw = 92.09, Sigma Aldrich) both mixed with ZnI_2 (Mw = 319.19, Fluorochem) to increase the fluid-fabric contrast by X-ray absorption [45]. The PEG based solution was the same as previously employed in Ref. [43], with fluid formulation: 62.5 wt% of water, 11.0 wt% of PEG, 22.6 wt% of ZnI_2 and 3.9 wt% of Kodak PhotoFlow 200. The glycerol-based solution was designed to obtain a viscosity close to that of the PEG solution at 24 °C and to present a similar X-ray attenuation degree. Since it was sought to have different wetting properties between the two fluids, no surfactant was added in the second solution and the final composition of the mix was: 62.5 wt% of glycerol, 20.1 wt% of ZnI_2 and 17.4 wt% of water. The physical properties of the two fluids are listed in Table 1. Viscosities were measured in continuous shear mode in a concentric rheometer (AR2000ex, TA Instrument) by means of a Peltier Couette setup with a temperature ramp ranging from 18 °C to 30 °C at 0.1 °C/min at a constant shear-rate of 10 s^{-1} (Fig. 2). The viscosity versus temperature dependence was fitted with an Arrhenius law:

$$\eta(T) = Bexp\left[-\frac{E_a}{RT}\right] \quad (4)$$

with B and E_a being fitting parameters. Both model fluids were Newtonian fluids with no change in properties during the time scale of the experimental observations. The surface tension in air at ambient temperature was measured with a Drop Shape Analyzer (DSA30, Krüss) by means of the pendant drop method.

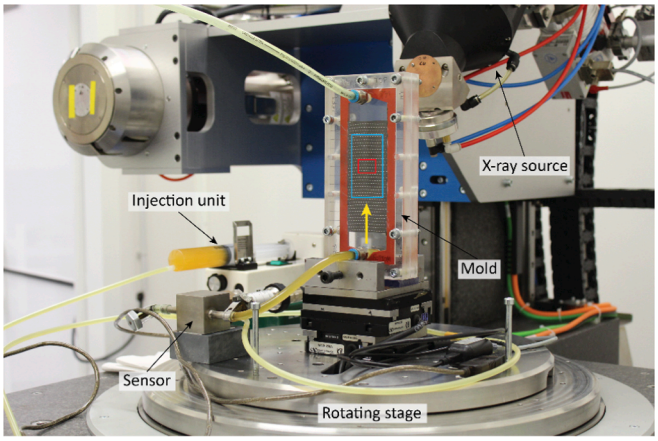

Fig. 3. Impregnation setup and X-ray imaging system. The yellow arrow shows the infiltrating direction, the blue rectangle the total 2D scan area and the red the 3D scan area. (For interpretation of the references to color in this figure legend, the reader is referred to the web version of this article.)

2.2. Static contact angle measurement

Static contact angles for the fabric/fluid systems were measured following the drop-on-fiber method: a single fiber was separated from a tow and taped straight to a metal frame. The liquid was then sprayed manually onto the fiber and the droplets were analyzed by a Keyence VHX-7000 microscope equipped with a zoom lens (100x to 1000x). Pictures were recorded with a resolution 1600 × 1200 pixels and a 4.18 pixel/μm ratio. Symmetrical droplets were selected, avoiding clam-shell shaped drops, and their length and height were measured as well as the fiber diameter and used as inputs for the estimation of the static contact angle following the geometrical analysis proposed by Carroll [46], which is the equivalent of the sessile drop method for flat plates.

2.3. Flow experiments

Flow experiments were performed with the setup shown in Fig. 3. Fibrous preforms, used as received, were prepared by stacking 9 layers of accurately hand-cut fabric with a dimension of 4.95 ± 0.05 cm × 10 cm. To accurately measure the volume fraction, the fabric stack was weighed with a scale (with a repeatability of ± 0.001 g). To avoid stray fibers, the sides of the fabric layers were kept in place with a small amount of sprayed adhesive. Then, layers were fitted in the cavity of a poly(methyl methacrylate) spacer of 3.2 mm with an inner silicon joint to minimize race tracking and enclosed in between two thick mm PMMA halves. To prevent the mold from bending, the outer PMMA plates were fastened with twelve metal screws, leaving the 3D scan area free of high-density material, as observed on Fig. 3. From the 3D scans, the mold

Table 2
Impregnation experiments.

Test	Fabric	Fluid	V_f[%]	T[°C]	η[Pa•s]	u[mm/s]	Ca(•10^{-4})
1	UD	PEG	43.1	25.8	0.074	0.708	9.06
2	UD	PEG	42.9	26.6	0.072	0.244	3.06
3	UD	PEG	43.0	26.2	0.073	0.074	0.94
3rep	UD	PEG	43.1	26.5	0.072	0.074	0.93
4	UDM	PEG	42.2	26.1	0.073	0.077	0.99
5	TW	PEG	44.5	24.1	0.077	0.087	1.14
6	UD	Glycerol	42.9	24.0	0.078	0.626	4.24
7	UD	Glycerol	42.9	23.7	0.079	0.270	1.19
8	UD	Glycerol	43.2	24.1	0.077	0.070	0.47
9	UDM	Glycerol	41.6	24.0	0.078	0.073	0.51
10	TW	Glycerol	44.5	23.9	0.078	0.083	0.55

deflection was measured to be less than 2%. In-plane injections at a constant flow rate were performed vertically (from bottom to top, z-direction) thanks to an injection unit R-100E syringe pump from Razel Scientific Instruments. Prior to injection, the fluids were stirred for one night to ensure a homogenous distribution of the contrasting agents. We noticed that a small amount of entrapped air was present in the fluid, in particular in the PEG based solution, which was evaluated to be 0.3%, using a flow experiment without fabric. The pressure and temperature were monitored along the test with a Keller Series 35XHTT sensor placed close to the inlet. The impregnation mold and the pressure sensor were placed in a rotating stage for the 3D scans acquisition.

The fluid velocity was adjusted by controlling the pump setting and was estimated by measuring the averaged front progression from the 2D scans to account for the variations that can arise due to reinforcement inhomogeneity. A summary of the experimental campaign is given in Table 2, with the resulting fiber volume fraction V_f, flow front velocity u, average fluid temperature T with respective viscosity η and capillary number Ca, calculated with the superficial velocity $U = u(1 - V_f)$. After each experiment, the PMMA mold, screws and silicon joint were washed thoroughly with water and soap, dried and were ready for reuse.

2.4. Visualization technique

The flow progression was visualized by 2D X-ray absorption at an imaging rate of 2 images per second using a laboratory X-ray micro-tomograph (RX Solutions Ultratom, PIXE Platform, EPFL, Switzerland) at 80 kV and 230 μA. Exposure time was thus 0.5 s, for the fastest experiments ran in this work, the flow could move up to 0.35 mm during one frame, leading to potential blurring of the features in these extreme cases. Images were acquired at a pixel size of 15 μm and the flow front was tracked for an area of approximately 5.5 cm long and 3 cm wide (blue area in Fig. 3). For that, three different positions were defined corresponding to three vertical movements of the X-ray source of 12 mm. A dry 2D scan was performed followed by the progressive acquisition of the impregnation (the number of acquisitions per experiment was set according to the flow speed) and finally by a wet 2D scan. Then, to acquire further information on the dry and wet states of the preform, before and after each impregnation, a tomographic 3D scan was performed at 3 images per second at a voxel size of 10 μm using the same X-ray facility. To reduce noise, a moving average of 4 frames was performed on the images, resulting in 1.33 s per image. The 3D scan was performed in the middle position of the 2D scans as illustrated in Fig. 3 with the red rectangle.

2.5. Unsaturated length measurement

From the 2D scans, a mean unsaturated length was measured for each experiment: images were cropped at three different locations with a width of 110 pixels for the UD fabric and 210 pixels for the twill, corresponding roughly to three bundles located in the middle and right and left sides of the image. Separate bundles were selected instead of a larger fabric width in order to only capture the unsaturated length arising from the capillary versus viscous forces competition and avoid effects such as race-tracking that would lead to non-flat fronts. Then, similarly to the procedure developed in Ref. [44], and as schematically shown in Fig. C1 of the supplementary information, the average pixel intensity value was calculated over the cropped area width and plotted versus the fabric length for each impregnation state as well as for the wet and dry states. By comparing the curves, two boundaries are set to define the unsaturated length.

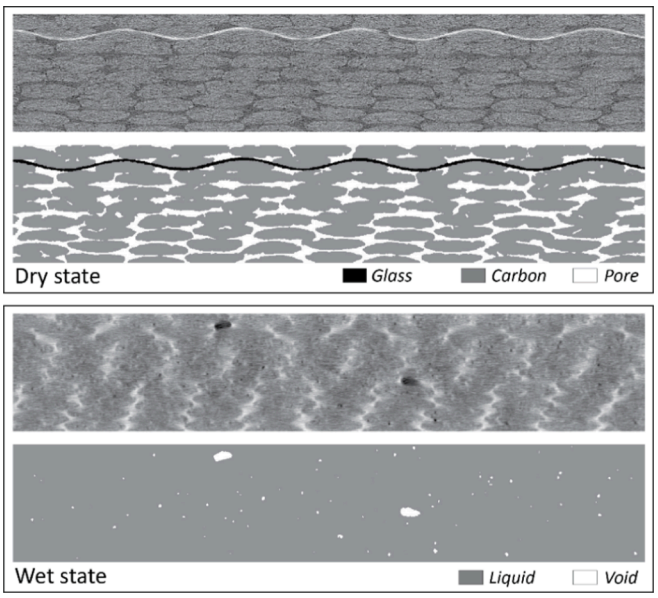

Fig. 4. Segmentation of two-dimensional cross-sections for dry and wet states of the UD carbon fabric (test #3).

2.6. 3D data segmentation

Scanned volumes were cropped to 1650 pixels × 310 pixels and 1200 slices, resulting in a volume size of 16.5 × 12.0 × 3.1 mm^3. The stack thickness was set to get rid of the mold and facilitate the segmentation analysis. An averaging filter was applied to the original data in the three x, y and z directions in Fiji [47]. Then, dry and wet scans were segmented by means of Ilastik [48], a machine-learning-based image analysis tool for pixel classification in which the user manually labels several regions corresponding to the different phases. Three segmentation training algorithms were developed, each using a volume of 100 consecutive slices that were manually labelled to generate the training data: one for the dry unidirectional fabric with “carbon”, “glass” and “pores” as labels; another for the dry twill with only two labels, namely “carbon” and “pores”; and one to treat the wet images with two phases “liquid” and “void”. An example of segmentation for dry and wet states for the UD fabric is illustrated in Fig. 4. The corresponding training algorithm is thereafter applied for each scan volume and segmented images were then assembled in Avizo software to analyze the void content, location, and geometry. In addition, a pore network model (PNM) construction was applied to the 3D segmented images, by using the PNM module from Avizo, to quantitatively assess the geometry and topology of the pore space. The segmented pore label, corresponding only to the *meso*-space in between bundles, was separated into different objects which were automatically assimilated to pores connected with pore-throats.

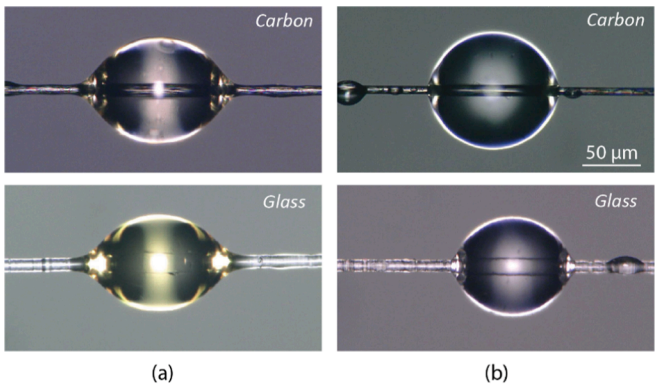

Fig. 5. Droplets of (a) the PEG-based and (b) glycerol-based model fluids on carbon and glass fibers.

3. Results

3.1. Evaluation of the static contact angles

To assess the static contact angle between carbon and glass fibers and the two model fluids, 20 to 25 droplets were analyzed for each condition. An example of droplet shape for each fiber/fluid system is shown in Fig. 5. The contact angle corresponds to the angle between the fiber surface and the resin, close to the air/fiber/resin interface, and is calculated as indicated in section 2.2, from the drop length and height. For the model fluid with PEG, a static contact angle of 23.42° ± 4.36° was obtained for carbon, and for glass 10.25° ± 5.61° (Fig. 5a). For the glycerol solution, a static contact angle of 52.54° ± 4.66° was obtained for carbon, and 41.35° ± 5.07° for glass (Fig. 5b). Hence, the PEG solution has a stronger static wetting behavior when compared to the glycerol towards the fiber surfaces.

3.2. Front displacement behavior in the UD carbon fabric

The morphological characteristics of the two model fluids displacements inside the unidirectional carbon preform under the different injection conditions (tests #1 to #3 and #6 to #9) were carefully explored. The videos of the progressive filling illustrating the flow patterns are provided as supplementary data A and for each experiment an example of the flow front morphology is presented in Fig. 6. The different patterns were elucidated by applying a variance filter and subsequently adding the filtered and original images. Strong capillary and viscous fingering from test #3 and #6 respectively as well as the simultaneous flow fronts are highlighted.

For the fastest injections (tests #1, $Ca = 9.06 \text{ X } 10^{-4}$ and #6, $Ca = 4.24 \text{ X } 10^{-4}$), the flow leads in between the tows, and thus is similar to drainage, in which the fluid has a non-wetting behavior, and the porous medium has a better affinity to the displaced fluid (air) when compared to the invading fluid (liquid). The flow progresses along the center of the largest pores as the fluid attempts to minimize the contact with the fibers, resulting in a viscous flow elucidated by the dominance of well-connected longitudinal paths in between the tows. This follows a piston-like advancement and the corresponding dominant pore-scale invasion mechanism under drainage condition is known in soil science as burst (or Haines jump) [49,50]. Moreover, where horizontal bundles are present, these longitudinal paths converge. The viscous fingering is as expected more significant for the less wetting fluid (test #6), where a clear domination of positive curvatures over negatives is observed, whereas for test #1, fingering is less pronounced, and the unsaturated

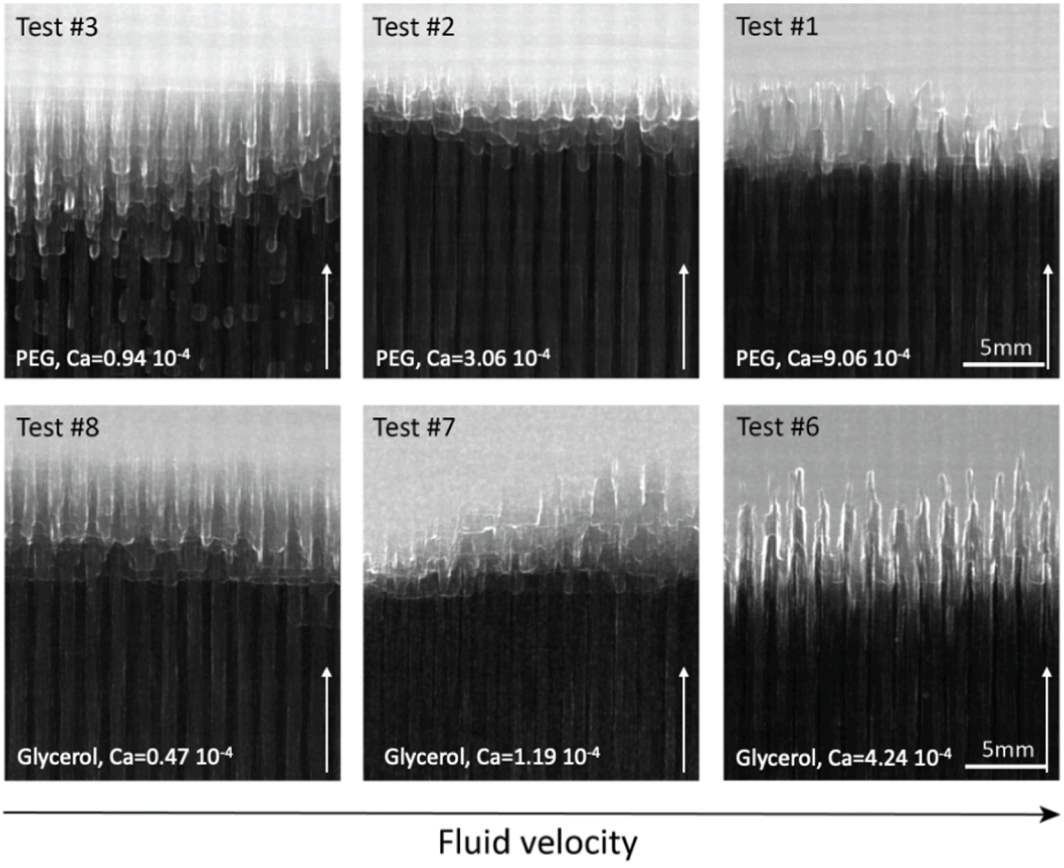

Fig. 6. Flow paths in the UD fabric impregnated with the PEG solution (tests #1 to #3) and the glycerol solution (tests #6 to #8) elucidated with a variance filter. The arrows indicate the direction of flow.

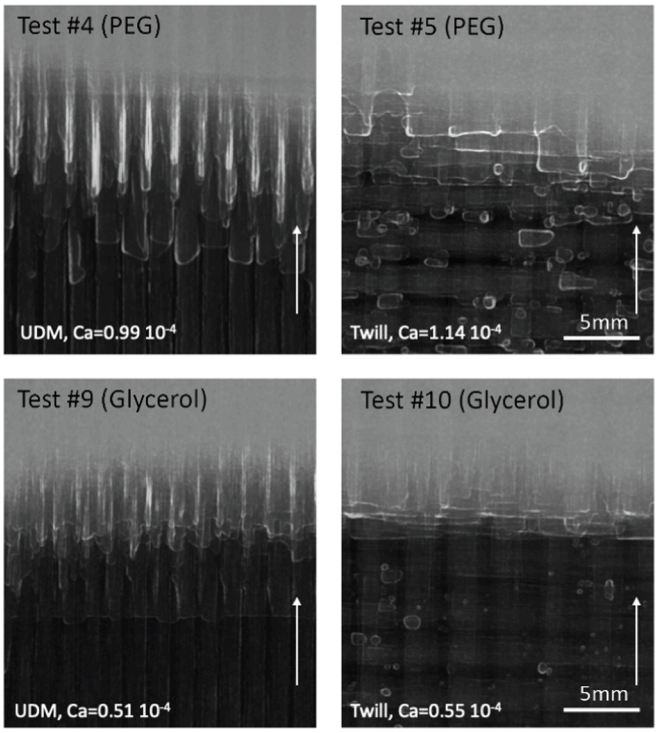

Fig. 7. Capillary dominated flow paths in UDM and TW fabrics impregnated with the PEG and glycerol solutions elucidated with a variance filter. The arrows indicate the direction of flow.

area is more compact.

For the intermediate cases, a rather balanced displacement is captured for both experiments #2, $Ca = 3.06 \text{ X } 10^{-4}$ and #7, $Ca = 1.19 \text{ X } 10^{-4}$. Capillary and viscous flows are hardly distinguished in the unsaturated length, and it is difficult to define sharp boundaries between the two displacement patterns. As matter of fact, we observe that there is an intermediate flow rate condition for which the fluid adopts both wetting behaviors at the same time depending on the displacement location. This can be linked to the variability in the pore distribution and the local heterogeneity with meso and micro-pores, which lead to the coexistence of different displacement mechanisms, regarded as a crossover pattern [51].

Finally, for capillary dominated cases (tests #3, $Ca = 0.94 \text{ X } 10^{-4}$ and #8, $Ca = 0.47 \text{ X } 10^{-4}$), the fluid invasion pattern is assimilated to an imbibition type. The flow progresses with a corner flow behavior, by filling pores with smaller cross section located inside the tows; the flow front is hence led by capillary wicking. As described by Bico et al. [52], two macroscopic fronts can be identified: ahead, a thin flow that propagates using the thin pore structure and at the bottom, a main flow which saturates the medium. For the strong wetting conditions (test #3), the unsaturated area is larger and the flow progresses less homogeneously as compared to test #8. As observed in the literature, a high wetting together with a low surface tension makes the air/fluid interfaces very easy to deform and stretch resulting in very unstable interfaces, resulting either in local fluid fast advance to re-equilibrate itself or in snap-off events, resulting in air entrapment [53–55]. Moreover, *meso*-void formation was not observed in the delayed front and took place where horizontal stitches were present, demonstrating that the porous medium geometry also plays an important role on the location and shape of entrapped voids. Then, test #8 falls in a less wetting condition, and even if capillary wicking is significant in the tows, the flow progresses backwards with a rather cooperative behavior and no snap-off events occur. The horizontal stitches were found to act as barriers, leveling and redistributing the delayed viscous flow.

As a summary, the pore-scale displacements for drainage and imbibition descriptions differ and these cannot be considered as "symmetric" phenomena. This difference stems from the pore-scale wetting. For drainage, the pore size distribution is the main geometrical factor dominating flow according to literature, which results in the present case to a vertical viscous fingering since *meso*-pores in the UD fabric are found along the flow direction. Conversely, for imbibition cases, the corner flow pattern impedes viscous fingering and the fluid front progresses inside the tows. Thus, the fluid front is in addition to the pore structure also influenced by the pores' geometrical shape, and their specific surface area as shown in Ref. [19].

3.3. Comparison of front displacements in the UD modified and the twill fabrics

Since previous results proved that horizontal bundles significantly affect the flow pattern and increase the occurrence of snap-off events, the effect of the fabric geometry on the flow progression and void entrapment in wetting conditions was investigated. For that, two approaches were selected: the structure of the UD carbon was modified to observe the effect of the transverse glass tows and a twill fabric was selected to highlight the influence of a more balanced geometry. The flow patterns obtained by impregnating both fabrics with the two fluids are shown in Fig. 7.

The UDM impregnations (tests #4, PEG, $Ca = 0.99 \text{ X } 10^{-4}$ and #9, Glycerol, $Ca = 0.51 \text{ X } 10^{-4}$) confirmed that horizontal bundles act as obstacles, blocking temporarily the vertical flow taking place in the *meso*-spaces. Then, once the flow overcomes the stitches, the delayed flow front speeds up locally to find stability, resulting in a large saturation gradient along the bundles. Thus, as already observed for the UD fabric (tests #3, PEG, $Ca = 0.94 \text{ X } 10^{-4}$ and #8, Glycerol, $Ca = 0.47 \text{ X } 10^{-4}$), the transverse yarns contribute to locally redistribute the fluid. Just behind the flow front, both cases exhibit a similar unsaturated area which as expected is longer when compared to simple UD impregnations since the distance between transverse stitches was increased, while the flow patterns and fluid distribution differ. For the strong wetting fluid (test #4), concave menisci in between the tows and in the delayed front progression are observed. In addition, when the fluid arrives to the

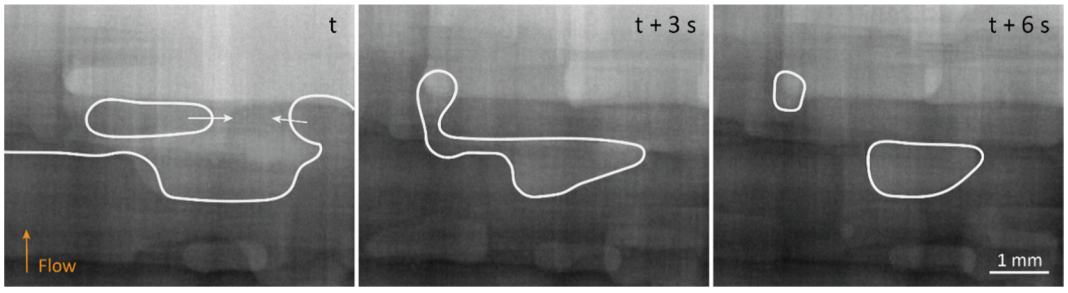

Fig. 8. Example of snap-off and break up from test #5 (Twill, PEG, $Ca = 1.14 \text{ X } 10^{-4}$) from three pictures taken at successive times. The arrows at time *t* indicate the local flow direction.

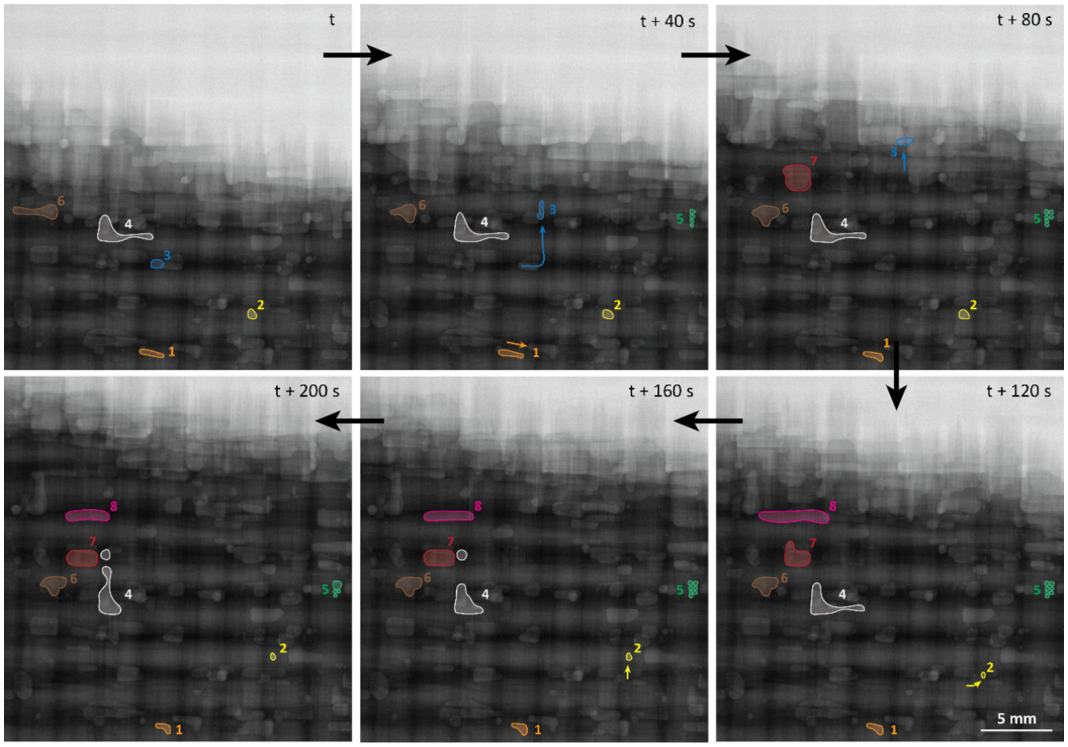

Fig. 9. Void motion in the TW fabric under capillary dominated flows (from test #5: Twill, PEG, $Ca = 1.14 \text{ X } 10^{-4}$). Flow direction is from bottom to top.

horizontal glass bundles, those start to be impregnated increasing the probability of snap-off events. This is similar to what happened in test #3 with pristine UD but less frequently. For the less wetting fluid (test #9), the delayed front, behind the capillary wicking, progresses also with concave menisci while with a more "U" shape, indicating a larger contact angle. The overall flow progression seems to be more cooperative whereas for test #4 the fluid front seems to be made up of individual fronts confirming previous observations.

Impregnation of the twill fabric was also performed under capillary dominated flow (tests #5, PEG, $Ca = 1.14 \text{ X } 10^{-4}$ and #10, Glycerol, $Ca = 0.55 \text{ X } 10^{-4}$). This fabric was chosen for its strong bi-directionality and its different *meso*-porosity (bundles are less compact leading to larger inter-tow space when compared to the UD). Evidently, this fabric architecture led to an increased void formation for both experiments as observed in Fig. 7, with a higher void fraction for the strongly wetting fluid (test #5). Snap-off events were found to arise from the early liquid progression inside the horizontal bundles, leading to an encirclement of air as represented in Fig. 8. The void shape differs between the two wetting conditions, namely, more elongated for the very wetting fluid, given the low surface tension and more round for the less wetting case.

3.4. Void motion phenomena

During the capillary dominated flows experiments, void motion (e.g. a change of void shape and size as well as void migration) was observed, in particular, with high frequency for the TW fabric and almost null for the two UD fabrics. An example of the different phenomena observed is presented in Fig. 9, in which the displacement of different bubbles has been tracked.

The evolution of pink, red and brown (8, 7 and 6 respectively) bubbles is illustrated just after their formation at the flow front; in this case, the void rearranges itself and shrinks to minimize the surface tension. The white (4) void undergoes a change of shape and size due to two consecutive splitting occurrences. Given its position and shape, this bubble seems to be not very stable, and the vertical fraction of the bubble along the fluid direction exerts a pressure on the bubbles that promotes the deformation and then break up. The blue (3) and yellow (2) voids illustrate a vertical migration through the preform in the fluid direction which are displaced thanks to the increasing fluid pressure with time in the constant flow rate experiments [6]. The blue (3) one, reaches the flow front and disappears whereas the yellow (2) one stays entrapped probably due to a channel constriction as illustrated in Fig. 10. Similarly, the orange (1) void migrates over a small distance and interestingly in an opposite direction to the flow, it ends trapped with a different shape from the initial one. Finally, green (5) bubbles show the formation of several rather small bubbles that are positioned first side by side, and with time end up coalescing. As a conclusion of this observation, several concomitant phenomena are observed during the same slow flow experiment, depending on the initial size of the bubble, its shape and location with respect to the transverse bundles.

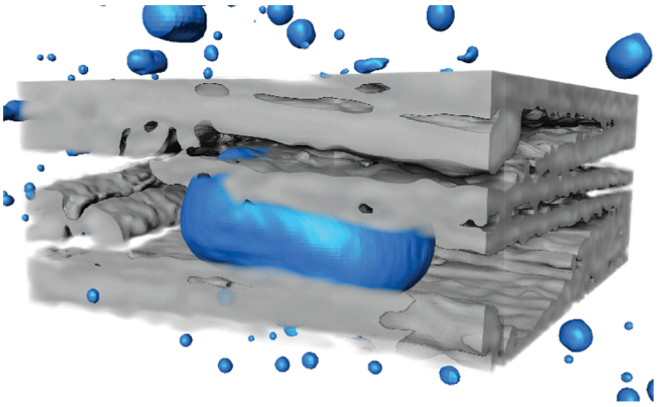

Fig. 10. 3D view of an entrapped void in a channel constriction (from test #10, Twill, Glycerol, $Ca = 0.55 \text{ X } 10^{-4}$)).

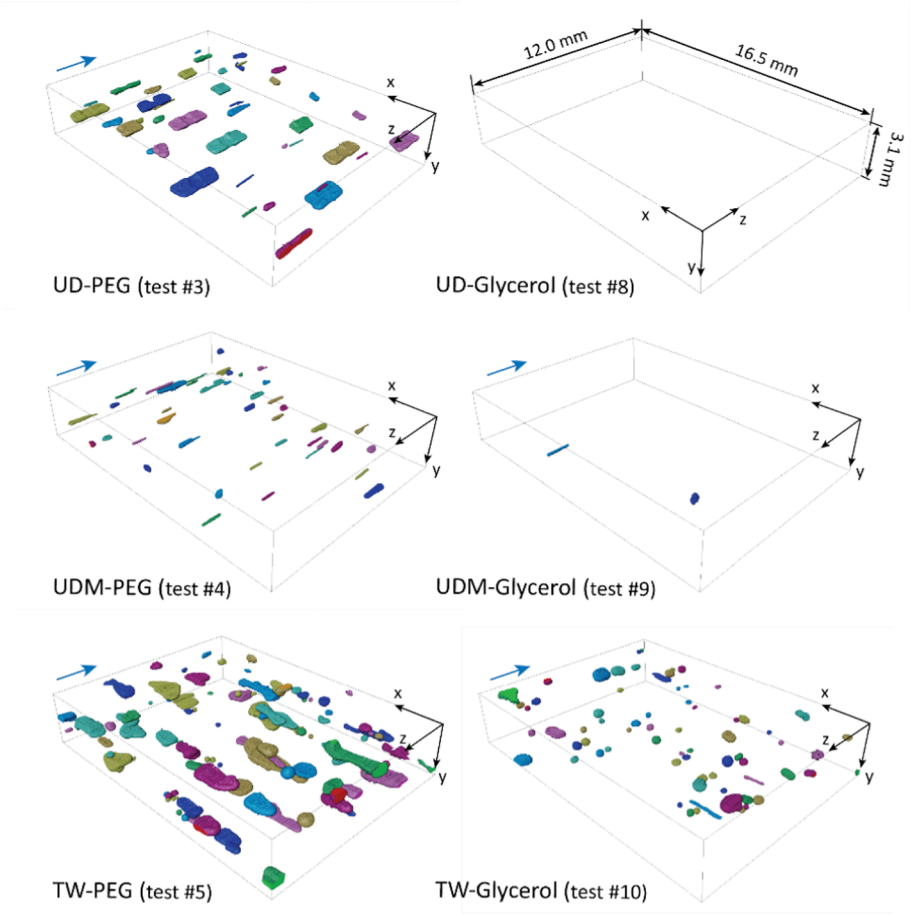

Fig. 11. 3D volume rendering of *meso*-void distribution for capillary driven tests. For the PEG experiments, *Ca* is in the range of 1 X 10^{-4}. For the Glycerol ones, *Ca* is in the range of 0.5 X 10^{-4}. The flow direction is indicated with the blue arrows. The colors were used to differentiate and label the voids. (For interpretation of the references to color in this figure legend, the reader is referred to the web version of this article.)

3.5. Void morphology and location

The porosity was segmented from the 3D wet scans. For all cases of capillary driven impregnation, *meso*-voids with a volume higher than 0.007 mm^3 are presented in Fig. 11. The figures of *meso*-voids were combined with the 3D scans of the dry states, to illustrate their location and morphology within the pore space. These combined images are provided as supplementary data B. From Fig. 11, it is clear that highly wetting conditions (PEG solution) were more prone to create *meso*-voids when compared to the impregnations carried out with the less wetting glycerol fluid. Comparing the UD-PEG and the UDM-PEG experiments, all voids were longitudinally aligned with the flow direction, with an obvious decrease of void content and size for the UDM. Comparing TW samples, the voids showed a different shape, very elongated in the very wetting case (test #5, $Ca = 1.14 \text{ X } 10^{-4}$) and more spherical for the less wetting case (test #10, $Ca = 0.55 \text{ X } 10^{-4}$) as expected given the different static contact angles. For both experiments, the residual voids remained oriented perpendicular to the flow in between horizontal bundles showing that they mainly arise from the presence of these obstacles at 90°, and formed by air encirclement as shown in Fig. 8.

From the void analysis, it was found that *meso*-voids for the UD fabric (test #3, $Ca = 0.94 \text{ X } 10^{-4}$), were suprisingly located in between two specific layers as shown in Fig. 12a; this was caused by the location and superposition of horizontal bundles. In particular, *meso*-voids were observed to be clamped by two glass bundles in successive fabric layers which created a channel constriction that promoted the snap-off events. This particular geometry resulted from a specific stacking of fabric layers that led to this pore configuration hindering the flow. To verify this, experiment #3 was repeated by varying the stack procedure (test #3rep, $Ca = 0.93 \text{ X } 10^{-4}$), to intentionally avoid the superposition of two glass bundles in successive layers facing each other. The lower resulting void content is shown in Fig. 12b. This finding underlines the importance of studying flow displacements in real systems containing several layers, and the risks created by increased constrictions created by a very regular lay-up. Moreover, these results show the careful attention that should be paid in manual labor parts of composite processing such as fabric stacking.

Finally, we also tested the hypothesis of further void removal by increasing the time after infiltration is complete, letting the fluid flow, known as bleeding in general LCM practice. We did not observe further void movement, this was probably due to the rather low fluid pressure, which we could not increase in the present experiments (and this is often difficult in practice, for exampe in vacuum resin infusion).

3.6. Relation between void content and unsaturated length

For experiments carried out with the UD fabric at different injection conditions (tests #1 to #3 and #6 to #8), the total void content extracted from the wet state 3D scans as well as the unsaturated length measured on the 2D impregnations are plotted as a function of the capillary number (Fig. 13). It should be noted that, even though the superficial velocity was very close for each pair of experiments, namely slow (tests #1 and #6), intermediate (tests #2 and #7) and fast (tests #3 and #8), the *Ca* differed significantly between fluid types (as expected given the different surface tension values between fluids). In both cases, a drop in unsaturated length is observed when flow is more balanced,

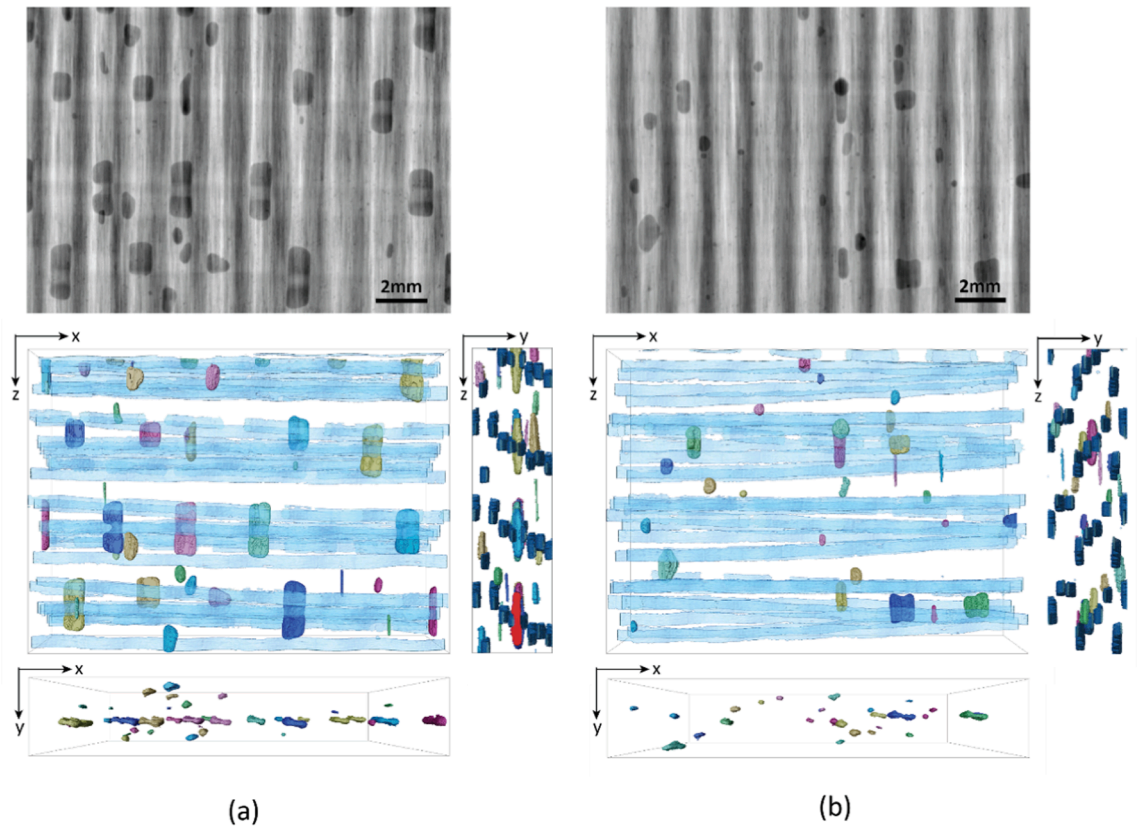

Fig. 12. Meso-void location in two UD fabric layers stacking configurations, 2D mean projection from the 3D scan of the wet state and segmented *meso*-voids and glass bundles (in blue): results from (a) test #3 (UD, PEG, $Ca = 0.94 \text{ X } 10^{-4}$) and (b) test #3rep (UD, PEG, $Ca = 0.93 \text{ X } 10^{-4}$). Flow is from bottom to top in the images in thex z plane. (For interpretation of the references to color in this figure legend, the reader is referred to the web version of this article.)

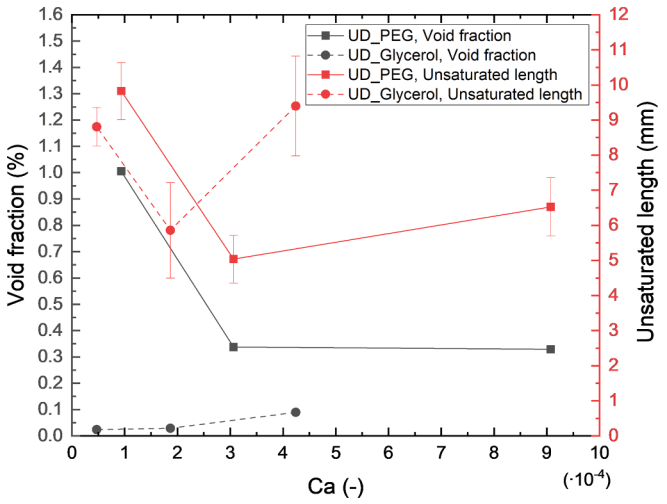

Fig. 13. Void fraction and unsaturated length resulting from the UD fabric impregnation with PEG and glycerol-based fluids as a function of capillary number.

however the trend of void fraction is not so clear. Nonetheless, what is clearly observed is that the nature of the fluid strongly affects the void content (Fig. 13, gray color).

Overall, the void content is higher for all the experiments performed with the PEG-based liquid. In particular, this liquid led to an increased number of micro-voids in the impregnated preforms for all conditions, with a baseline amount around 0.3%. In addition, impregnation with PEG solution led to an increased void content for the low-speed case due to the formation of *meso*-voids, whereas intermediate and viscous flow cases led to a similar void content. For the fastest flow (test #1, $Ca = 9.06 \text{ X } 10^{-4}$), the viscous fingering was indeed not prominent, the flow displacement being thus classified as a rather low drainage or even cross-flow pattern. For impregnation with the glycerol solution, the number of voids is very low for both slow and intermediate speeds and voids start to appear when the velocity is increased, in the form of micro-voids due to the pronounced viscous fingering and delayed flow in the tows. As already observed optically in pristine and fluorine coated glass fabrics by Yoshiara et al. [34], by increasing the static contact angle (in our case from PEG to glycerol), the *meso*-void formation is suppressed even for small *Ca*.

A direct relation between the void content and the unsaturated length is not so simple to establish apart from the fact that the smallest unsaturated area corresponds to a reduced void content as flow speeds in inter- and intra-tow regions are close. Then, for both cases of slow impregnation (low *Ca* value), the unsaturated lengths were very similar (around 9.5 mm ± 1 mm), however, an increased void content was obtained with the PEG solution as a corner flow, stemming from its low surface tension enhanced the formation of *meso*-voids as already

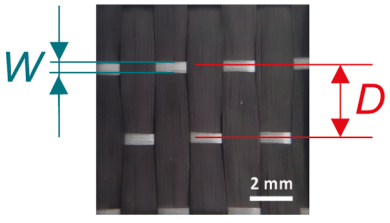

Fig. 14. Example of inter-bundle distance (*D*) and bundle width (*W*) measurement on the UD fabric.

Table 3
Inter-bundle over bundle width results.

Fabric	D[mm]	W[mm]	W/D[-]
UD	3.37 ± 0.10	0.53 ± 0.03	0.16
UDM	10.07 ± 0.28	0.53 ± 0.03	0.05
TW	2.97 ± 0.42	2.37 ± 0.37	0.80

discussed. This shows the importance of pore-scale kinetics and its influence at Darcy's scale.

Similarly, the unsaturated length was plotted versus void content as a function of the capillary number for the UD, UDM and TW fabric impregnations, Fig. C2 in the supplementary information.

With the aim of investigating the effect of the fabric geometry on the flow kinetics, a dimensionless number was defined for each fabric type to account for the crossover events describing potential obstacles to the flow. The bundle width (W) over the average distance between successive transverse yarns (D) was calculated as illustrated in Fig. 14. The ratio W/D gives a value between 0 and 1: if W/D is close to 0, the fabric is more unidirectional with thin horizontal bundles, and conversely, if W/D is close to 1, the fabric shows a bidirectional architecture with thick perpendicular bundles.

The inter-bundle distance (D) and bundle width (W) were measured on a fabric over an average of 15 measurements performed by a caliper and under an optical microscope respectively. The results are presented in Table 3 and the ratio W/D was plotted versus void content and unsaturated length in Fig. 15 (for an easier interpretation, the data projection was also plotted).

Analyzing the unsaturated length versus void content, taking the UD fabric as reference (dots in Fig. 15), when the preferential bundle direction was increased by removing some horizontal stitches (UDM), less voids were entrapped, and a larger unsaturated length and standard deviation is observed on account of the larger space between horizontal bundles (Fig. 15, green arrows). Thus, in a more unidirectional fabric (with fibers and tows aligned with the flow direction), even though the flow does not progress with the same speed in intra and inter-tow regions, few voids are created because the flow is not hampered by any obstacles such as transverse bundles or notable channel constrictions. Conversely, fiber bundles oriented with an angle to the flow direction triggered more voids and a smaller unsaturated area, as illustrated with the TW fabric (Fig. 15, blue arrows). In this case, horizontal bundles act as flow barriers, responsible for snap-off events and leveling the flow front thus reducing the unsaturated length. Hence, the results confirm that the topology of the porous medium plays a major role in governing flow and influencing void entrapment events and the extent of unsaturated pore space. It is thus observed that a larger unsaturated area is not strictly linked to an increased void content.

An increase of the W/D ratio results in a decrease of the unsaturated length (Fig. 15, pink arrow) and an increase of the void content (Fig. 15, orange arrow). This trend shows that thick bundle widths horizontal to the flow direction are determinant to the void formation mechanisms. By comparing values of Table 3, UD and TW fabrics have a similar inter-

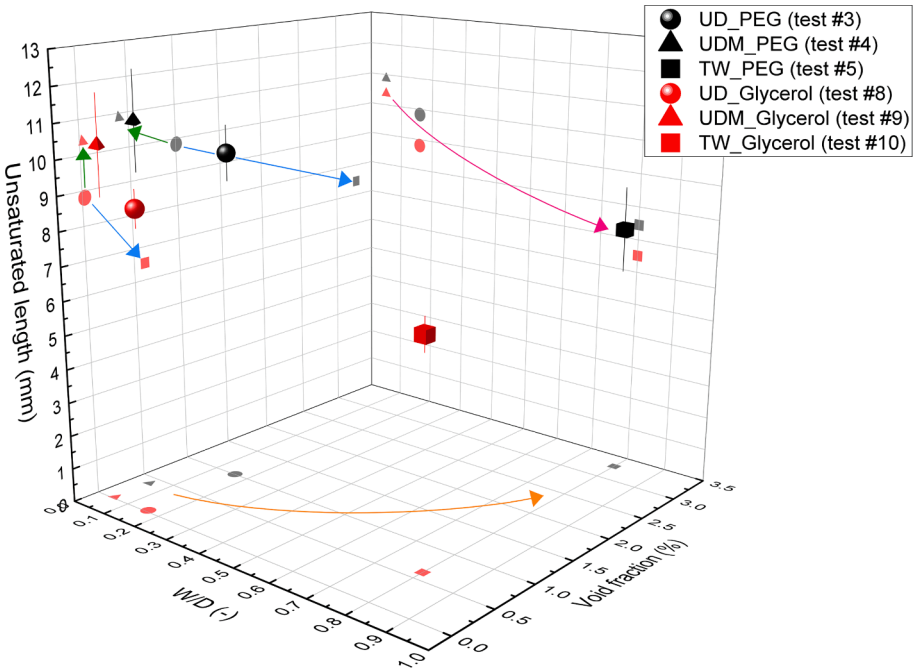

Fig. 15. Unsaturated length versus void fraction and the W/D ratio for the low speed impregnation of the UD, UDM and TW fabrics.

Table 4
Pore network model results.

Test #	Fabric/Liquid	Pore-body eq. radius [mm]	Pore-throat eq. radius [mm]	Pore-throat length [mm]	Coordination number	Number of pores	Number of throats
3	UD/PEG	0.31 ± 0.11	0.11 ± 0.06	1.57 ± 0.89	4.91 ± 2.44	763	1869
3rep	UD/PEG	0.32 ± 0.10	0.11 ± 0.06	1.58 ± 0.87	4.99 ± 2.22	712	1775
4	UDM/PEG	0.31 ± 0.11	0.11 ± 0.07	2.11 ± 1.47	4.52 ± 2.01	534	1208
5	TW/PEG	0.40 ± 0.14	0.15 ± 0.09	1.78 ± 0.77	4.38 ± 2.13	405	887
8	UD/Glycerol	0.28 ± 0.09	0.10 ± 0.05	1.49 ± 0.89	3.57 ± 2.11	896	2046
9	UDM/ Glycerol	0.32 ± 0.10	0.11 ± 0.07	2.14 ± 1.33	3.83 ± 2.01	467	895
10	TW/Glycerol	0.40 ± 0.05	0.14 ± 0.08	1.80 ± 0.78	4.52 ± 1.15	399	902

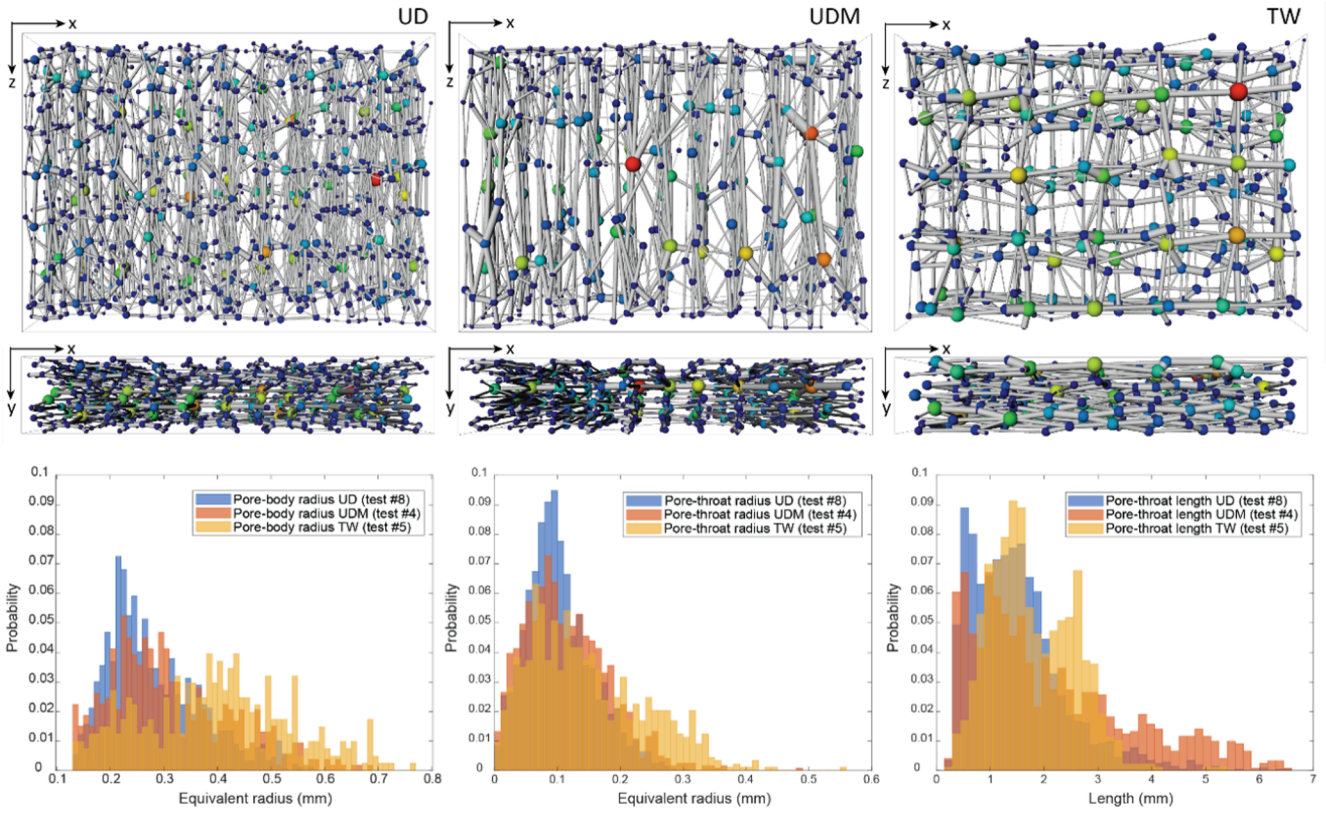

Fig. 16. 3D views of the pore-network of the scanned fabrics (UD (test #8), UDM (test #4) and TW (test #5) and corresponding histograms for the pore-body and pore-throat radii as well as pore-throat lengths. The pore bodies and pore throats are respectively rendered as colored spheres and gray cylinders that are smaller than their actual sizes to improve visualization. For both pores and throats, the size is related to the equivalent pore size (scale factor 0.5) and for the pores, the color distribution is in relation to the pore volume (from dark red corresponding to large pores and dark blue smaller pores). (For interpretation of the references to color in this figure legend, the reader is referred to the web version of this article.)

bundle width, but since the horizontal tow is thicker for the TW, this makes a higher obstacle and barrier for the flow which creates abrupt path changes (90° from the unidirectional flow direction to the horizontal tow), promoting the number of snap-off events. Moreover, increasing the number of horizontal bundles makes longitudinal tows to be wavier, influencing the nesting and having a direct effect on the *meso*-pore connection in between layers.

3.7. Pore network modelling

Owing to the fabric architecture impact on void entrapment events in particular for capillary driven flows, a pore network model, characterizing the connectivity and pores size, is applied to better describe the *meso*-pore space in 3D for preforms of tests #3 to #5 and #8 to #10. The statistical results for the different properties of the pore-network, namely the pore-body and pore-throat radii, the pore-throat length and pore network connectivity (measured as the coordination number defined as the number of throats over the number of pores within the network) for all samples are presented in Table 4 [39,56].

Similar results were obtained for the same fabric types (UD, UDM and TW) as expected. For this reason, only one example of pore network construction per fabric configuration is shown in Fig. 16 as well as the corresponding histograms of the pore-body and pore-throat radii and the pore-throat length distribution. The predominance of unidirectional throats is observed in both UD and UDM, while TW presents a grid type topological description of the medium, with several horizontal throats. The pore-body histogram is very similar for both UD and UDM samples, indicating that the pore size did not change much by modifying the fabric, whereas the twill configuration led to a higher mean value of pore-radius as well as a wider distribution. The pore-throat distribution is very similar for the three fabrics but the pore-length differed, in particular, for the UDM fabric for which the throats were longer when compared to UD or TW fabrics.

The twill fabric has a pore size distribution that is shifted to the larger sizes, triggering a more heterogeneous pore architecture influencing the spatial scaling effects and increasing the probability of trapping events which is in line with our previous results. Conversely, UD and UDM show a more homogeneous architecture, resulting in less trapping as observed in the experiments and it is expected that this pore topology would facilitate the upscaling from pore description to macro flows in a modelling point of view. For the UD fabric, it is interesting to note that the mean pore radius was measured to be around 300 μm (pore body equivalent radius from the PNM, Table 4), whereas the distance between tows as observed from the surface is about 60 μm (measured from a micrograph). This indicates that the fabric *meso*-spaces are dominated by the spaces between layers, in regions where the glass stitches create locally more compressed tows.

Similarly to the descriptor W/D ratio in 2D, we explored to describe the 3D configuration in terms of crossover events. In particular, the quantitative analysis of the throat geometry and distribution illustrates the capacity of fluid transport into the pore network [57]. This is why, on one side, the throat volume was calculated, as the throat area times the throat length, since it will be proportional to the volumetric rate of fluid that the throats will drain and on the other side, the orientation of the throats with respect to the flow direction was measured by calculating the angle between the z-direction and each single throat in the xz plane. In Fig. 17, the 3D histogram of the throat volume and the resulting angle is plotted for each fabric type. Between the UD and UDM fabrics, the main orientation in the 0° is demonstrated by a wider distribution of throat volume close to the 0° for the UDM as expected. For

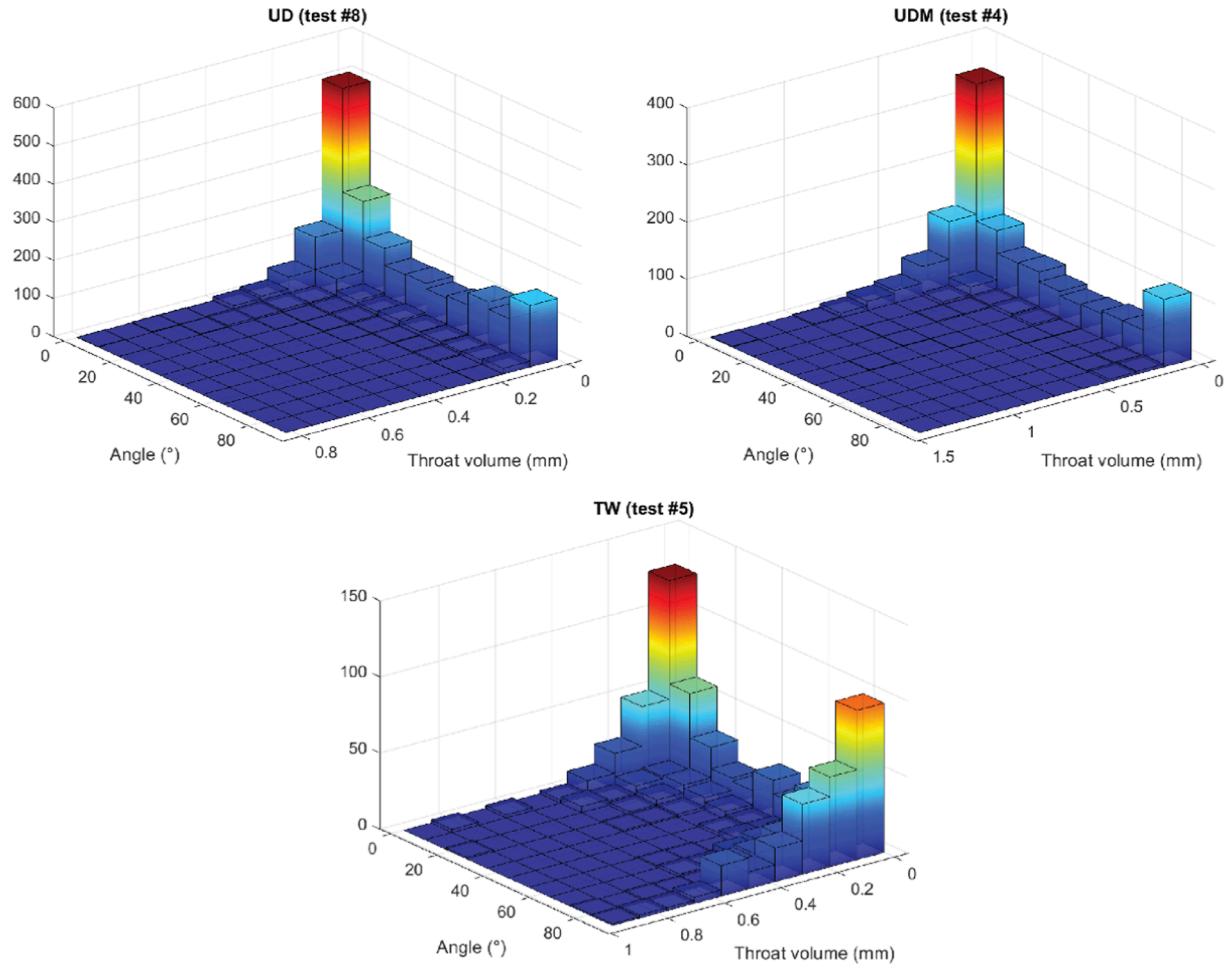

Fig. 17. 3D histograms of the angle of throats with respect to the z-direction and the throat volume for UD, UDM and TW fabrics.

these fabrics, above 20°, there is a more or less constant distribution of throat volumes. TW fabric with similar proportion of throat volume at 0° and 90° confirm the strong bi-directionality. Moreover, for this type of fabric there are really no throats oriented around 45°, when compared to the other fabrics, proving the abrupt corners that the flow will have to face. Finally, it is worth noting that the pore characteristics are very similar for tests #3 and #3rep as shown in Table 4, apart from a slightly smaller number of pores and throats, whereas we observed a different final porosity attributed to the superposition of transverse tows. This indicates some of the limitations of the pore network approach, and the possible need for more accurate descriptors of the presence and nature of transverse constrictions.

4. Conclusion

Although resin infiltration is controlled by the porous medium permeability, the infiltration speed and viscosity, according to Darcy's law, it is known that the wettability also plays an important role in multiphase flows since it controls the location and spatial distribution of flow patterns inside the porous media. In this study, we combined X-ray radiography and X-ray computed tomography to elucidate the link between dynamic fluid patterns, pore geometry and void entrapment mechanisms and proved the role of wettability in carbon fibrous preforms infiltration through experimental results enriched by advanced imaging techniques. In particular, we observed in-situ imbibition and drainage displacements in a UD fabric and imbibition displacements in a UD modified and a twill fabric employing two liquids with different static contact angles.

Pore-scale displacements, observed by 2D scans, differed between drainage and imbibition. In drainage, a piston like displacement in the *meso*-pores located between the tows leads the flow and vertical viscous fingering is observed. In imbibition, though, where fluid displacement is very slow, the wettability was found to play a crucial role in the progression of the flow front and void entrapment mechanisms. In particular, a very strong wetting system results in a strong corner fluid flow type triggering a less cooperative progressive flow front, enhancing the probability of snap-off events [58].

The 3D scan of the wet state allowed measurement of the void content and segmentation of the *meso*-porosity to investigate and compare the void morphology (highly influenced by the contact angle) and location in space. We were able to bring out that the UD fabric stack led to a particular porous morphology that influenced void entrapment in between 2 layers that present a specific pore configuration. Then, by comparing the void content for the capillary impregnations of the UD, UDM, and TW fabrics, the pore space configuration showed to significantly influence the amount of air trapping events. Moreover, it was found that bundles oriented perpendicular to the flow act as "obstacles" that can increase the probability for snap-off events as well as "stoppers" leveling off the flow and decreasing the unsaturated length. A dimensionless number was calculated in 2D in a single fabric layer to account for the bundle width over the inter-bundle distance. A pore network model (PNM) was in addition applied to the segmented 3D scans of the dry state, to better describe these three *meso*-pore architectures and two major geometrical parameters were found to affect capillary trapping: a wide pore (body and throat) size distribution together with and throat angle farther from the flow direction. The PNM approach could be

further exploited to predict fluid patterns and susceptible locations for void entrapment events even though this would require a more localised analysis, and a higher resolution 3D scan to fully capture the intra-tow flow [59].

This work presents a complete methodology to assess fluid displacement in fibrous porous media and leaves the door open to perform a deeper analysis on the effect of wettability and pore geometry on void formation mechanisms. Next steps would be to determine how the *Ca* versus void content curve evolves as a function of the wettability and to further investigate the link between the fabric geometry and void entrapment mechanisms with the PNM approach by studying other fabric types for example (i.e. non-crimp or knitted fabrics among others) with the aim of quantitatively describing the optimal capillary number Ca_{opt}.

CRediT authorship contribution statement

Helena Teixidó: Investigation, Methodology, Software, Validation, Writing – original draft. **Baris Caglar:** Methodology, Supervision, Formal analysis, Writing – review & editing. **Véronique Michaud:** Conceptualization, Funding acquisition, Project administration, Supervision, Writing – review & editing.

Declaration of Competing Interest

The authors declare that they have no known competing financial interests or personal relationships that could have appeared to influence the work reported in this paper.

Data availability

Data are available in a repository, links procided in the supplementary information.

Acknowledgments

This work was supported by the Swiss National Science Foundation, Switzerland (SNF n° 200021_182669). The authors acknowledge the SMaL laboratory at EPFL for use of their Drop Shape Analyzer.

Appendix A. Supplementary material

Supplementary data to this article can be found online at https://doi.org/10.1016/j.compositesa.2023.107733.

References

[1] Bear J. Modeling phenomena of flow and transport in porous media. Springer; 2018.
[2] Stokes JP, Weitz DA, Gollub JP, Dougherty A, Robbins MO, Chaikin PM, et al. Interfacial stability of immiscible displacement in porous medium. Phys Rev Lett 1986;57:1718–21. https://doi.org/10.1103/PhysRevLett.57.1718.
[3] Huang PW, Flemisch B, Qin CZ, Saar MO, Ebigbo A. Relating Darcy-scale chemical reaction order to pore-scale spatial heterogeneity. Transp Porous Media 2022;144:507–43. https://doi.org/10.1007/s11242-022-01817-0.
[4] Rücker M, Berg S, Armstrong RT, Georgiadis A, Ott H, Schwing A, et al. From connected pathway flow to ganglion dynamics. Geophys Res Lett 2015;42:3888–94. https://doi.org/10.1002/2015GL064007.
[5] Park CH, Il LW. Modeling void formation and unsaturated flow in liquid composite molding processes : a survey and review. J Reinf Plast Compos 2011;30:957–77. https://doi.org/10.1177/0731684411411338.
[6] Mehdikhani M, Gorbatikh L, Verpoest I, Lomov S, v.. Voids in fiber-reinforced polymer composites : A review on their formation, characteristics, and effects on mechanical performance. J Compos Mater 2018. https://doi.org/10.1177/0021998318772152.
[7] Lenormand R, Touboul E, Zarcone C. Numerical models and experiments on immiscible displacements in porous media. J Fluid Mech 1988;189:165–87. https://doi.org/10.1017/S0022112088000953.
[8] Guo H, Song K, Hilfer R. A Brief Review of Capillary Number and its Use in Capillary Desaturation Curves. Transp Porous Media 2022;144:3–31. https://doi.org/10.1007/s11242-021-01743-7.
[9] Lebel F, Fanaei AE, Ruiz E. Prediction of optimal flow front velocity to minimize void formation in dual scale fibrous reinforcements. Int J Mater Form 2014:93–116. https://doi.org/10.1007/s12289-012-1111-x.
[10] Leclerc JS, Ruiz E. Porosity reduction using optimized flow velocity in Resin Transfer Molding. Compos A 2008;39:1859–68. https://doi.org/10.1016/j.compositesa.2008.09.008.
[11] Park CH, Lebel A, Saouab A, Bréard J, Il W. Modeling and simulation of voids and saturation in liquid composite molding processes. Compos A 2011;42:658–68. https://doi.org/10.1016/j.compositesa.2011.02.005.
[12] Ruiz E, Achim V, Soukane S. Optimization of injection flow rate to minimize micro / macro-voids formation in resin transfer molded composites. Compos Sci Technol 2006;66:475–86. https://doi.org/10.1016/j.compscitech.2005.06.013.
[13] Michaud V. A Review of Non-saturated Resin Flow in Liquid Composite Moulding processes. Transp Porous Media 2016. https://doi.org/10.1007/s11242-016-0629-7.
[14] Verrey J, Michaud V, Manson JA. Dynamic capillary effects in liquid composite moulding with non-crimp fabrics. Compos A Appl Sci Manuf 2006;37:92–102. https://doi.org/10.1016/j.compositesa.2005.04.011.
[15] Balbinot C, Martoïa F, Dumont PJJ, Orgéas L, Bloch JF, Rolland du Roscoat S, et al. In situ 3D observations of capillary-driven flows in parallel arrangements of rigid fibres using X-ray microtomography. Compos Part A Appl Sci Manuf 2022;157. https://doi.org/10.1016/j.compositesa.2022.106941.
[16] Teixidó H, Staal J, Caglar B, Michaud V. Capillary effects in fiber reinforced polymer composite processing: a review. Front Mater 2022;9:1–24. 10.3389/fmats.2022.809226.
[17] Guo X, Liu R, Wang J, Shuai S, Xiong D, Bai S, et al. Pore-scale modeling of wettability effects on infiltration behavior in liquid composite molding. Phys Fluids 2020;32. https://doi.org/10.1063/5.0023161.
[18] Wang J, Fuentes CA, Zhang D, Wang X, Willem A, Vuure V, et al. Wettability of carbon fibres at micro- and mesoscales. Carbon N Y 2017;120:438–46. https://doi.org/10.1016/j.carbon.2017.05.055.
[19] Nhunduru RAE, Jahanbakhsh A, Shahrokhi O, Wlodarczyk KL, Garcia S, Maroto-Valer MM. The Impact of Wettability on Dynamic Fluid Connectivity and Flow Transport Kinetics in Porous Media. Water Resour Res 2022;58. https://doi.org/10.1029/2021wr030729.
[20] Zhao B, MacMinn CW, Juanes R. Wettability control on multiphase flow in patterned microfluidics. PNAS 2016;113:10251–6. https://doi.org/10.1073/pnas.1603387113.
[21] Geistlinger H, Ataei-Dadavi I, Mohammadian S, Vogel HJ. The impact of pore structure and surface roughness on capillary trapping for 2-D and 3-D porous media: Comparison with percolation theory. Water Resour Res 2015;51:9094–111. https://doi.org/10.1002/2015WR017852.
[22] Holtzman R. Segre E. Wettability stabilizes fluid invasion into porous media via nonlocal, cooperative pore filling 2015;115:164501. https://doi.org/10.1103/PhysRevLett.115.164501.
[23] Trojer M, Szulczewski ML, Juanes R. Stabilizing Fluid-Fluid Displacements in Porous Media Through Wettability Alteration. Phys Rev Appl 2015;3. https://doi.org/10.1103/PhysRevApplied.3.054008.
[24] Zhang L, Wang J, Fuentes CA, Zhang D, van Vuure AW, Seo JW, et al. Wettability of carbon nanotube fibers. Carbon N Y 2017;122:128–40. https://doi.org/10.1016/j.carbon.2017.06.027.
[25] Qiu S, Fuentes CA, Zhang D, van Vuure AW, Seveno D. Wettability of a single carbon fiber. Langmuir 2016;32:9697–705. https://doi.org/10.1021/acs.langmuir.6b02072.
[26] Pucci MF, Liotier P, Drapier S. Capillary effects on flax fibers – Modification and characterization of the wetting dynamics. Compos A 2015;77:257–65. https://doi.org/10.1016/j.compositesa.2015.03.010.
[27] Lee Y, Chiao S. Visualization of Dynamic Contact Angles on Cylinder and Fiber. vol. 181. 1996.
[28] Vega MJ, Seveno D, Lemaur G, Adão MH, de Coninck J. Dynamics of the rise around a fiber: Experimental evidence of the existence of several time scales. Langmuir 2005;21:9584–90. https://doi.org/10.1021/la051341z.
[29] Pucci MF, Liotier P, Drapier S. Capillary wicking in a fibrous reinforcement – Orthotropic issues to determine the capillary pressure components. Compos A 2015;77:133–41. https://doi.org/10.1016/j.compositesa.2015.05.031.
[30] Pucci MF, Liotier P, Drapier S. Capillary wicking in flax fabrics – Effects of swelling in water. Colloids Surf A Physicochem Eng Asp 2016;498:176–84. https://doi.org/10.1016/j.colsurfa.2016.03.050.
[31] Vo HN, Pucci MF, Corn S, le Moigne N, Garat W, Drapier S, et al. Capillary wicking in bio-based reinforcements undergoing swelling – Dual scale consideration of porous medium. Compos A 2020:134. https://doi.org/10.1016/j.compositesa.2020.105893.
[32] Neunkirchen S, Blößl Y, Schledjewski R. A porous capillary tube approach for textile saturation. Compos Sci Technol 2022;2:109450. https://doi.org/10.1016/j.compscitech.2022.109450.
[33] Caglar B, Tekin C, Karasu F, Michaud V. Assessment of capillary phenomena in liquid composite molding. Compos A 2019;120:73–83. https://doi.org/10.1016/j.compositesa.2019.02.018.
[34] Yoshihara K, Kamei Y, Mizuno A, Ohgaki H, Hori T, Ueno I. Effect of wettability on viscous fluid impregnation in single-layer woven- fibre bundles driven by pressure difference. Compos A 2020;138:106049. https://doi.org/10.1016/j.compositesa.2020.106049.
[35] Salvatori D, Caglar B, Teixidó H, Michaud V. Permeability and capillary effects in a channel-wise non-crimp fabric. Compos A 2018;108:41–52. https://doi.org/10.1016/j.compositesa.2018.02.015.

[36] Schell JSU, Renggli M, van Lenthe GH, Müller R, Ermanni P. Micro-computed tomography determination of glass fibre reinforced polymer meso-structure. Compos Sci Technol 2006;66:2016–22. https://doi.org/10.1016/j.compscitech.2006.01.003.
[37] Ali MA, Umer R, Khan KA, Cantwell WJ. Application of X-ray computed tomography for the virtual permeability prediction of fiber reinforcements for liquid composite molding processes: A review. Compos Sci Technol 2019:184. https://doi.org/10.1016/j.compscitech.2019.107828.
[38] Fatt I. The network model of porous media. Transactions of the AIME 1956;207:144–81. https://doi.org/10.2118/574-G.
[39] Xiong Q, Baychev TG, Jivkov AP. Review of pore network modelling of porous media: Experimental characterisations, network constructions and applications to reactive transport. J Contam Hydrol 2016;192:101–17. https://doi.org/10.1016/j.jconhyd.2016.07.002.
[40] Delerue JF, Lomov S, v, Parnas RS, Verpoest I, Wevers M.. Pore Network Modeling of Permeability for Textile Reinforcements. Polym Compos 2003;3:344–57.
[41] Li Y, Chi Y, Zhao C, Miao Y, Han S, Chen L. Modelling fluid flow in carbon fibre porous media based on X-ray microtomography and lattice Boltzmann method. Compos Struct 2022:300. https://doi.org/10.1016/j.compstruct.2022.116085.
[42] Li Y, Chi Y, Han S, Miao Y, Chen L. Investigation on CT characterization of pore structure in nylon-uncured rubber composite from a microscopic view. Sci Rep 2021;11:15682. https://doi.org/10.1038/s41598-021-95178-1.
[43] Teixidó H, Broggi G, Caglar B, Michaud V. Measurement and modelling of dynamic fluid saturation in carbon reinforcements. Compos A Appl Sci Manuf 2023::107520. https://doi.org/10.1016/j.compositesa.2023.107520.
[44] Teixidó H, Caglar B, Revol V, Michaud V. In-operando dynamic visualization of flow through porous preforms based on X-ray phase contrast imaging. Compos A Appl Sci Manuf 2021:149. https://doi.org/10.1016/j.compositesa.2021.106560.
[45] Sket F, Enfedaque A, Alton C, González C, Molina-Aldareguia JM, Llorca J. Automatic quantification of matrix cracking and fiber rotation by X-ray computed tomography in shear-deformed carbon fiber-reinforced laminates. Compos Sci Technol 2014;90:129–38. https://doi.org/10.1016/j.compscitech.2013.10.022.
[46] Carroll BJ. The Accurate Measurement of Contact Angle, Phase Contact Areas, Drop Volume, and Laplace Excess Pressure in Drop-on-Fiber Systems. J Colloid Interface Sci 1976;57:488–95.
[47] Schindelin J, Arganda-Carreras I, Frise E, Kaynig V, Longair M, Pietzsch T, et al. Fiji: An open-source platform for biological-image analysis. Nat Methods 2012;9:676–82. https://doi.org/10.1038/nmeth.2019.
[48] Berg S, Kutra D, Kroeger T, Straehle CN, Kausler BX, Haubold C, et al. ilastik: interactive machine learning for (bio)image analysis. Nat Methods 2019;16:1226–32. https://doi.org/10.1038/s41592-019-0582-9.
[49] Bakhshian S, Rabbani HS, Hosseini SA, Shokri N. New Insights Into Complex Interactions Between Heterogeneity and Wettability Influencing Two-Phase Flow in Porous Media. Geophys Res Lett 2020:47. https://doi.org/10.1029/2020GL088187.
[50] Hoogland F, Lehmann P, Mokso R, Or D. Drainage mechanisms in porous media: From piston-like invasion to formation of corner flow networks. Water Resour Res 2016;52:8413–36. https://doi.org/10.1002/2016WR019299.
[51] Guo X, Liu R, Wang J, Shuai S, Xiong D, Bai S, et al. 3D actual microstructure-based modeling of non-isothermal infiltration behavior and void formation in liquid composite molding. App Math Model 2021;94:388–402. https://doi.org/10.1016/j.apm.2021.01.018.
[52] Bico J, Quéré D. Precursors of impregnation. Europhys Lett 2003;61:348–53. https://doi.org/10.1209/epl/i2003-00196-9.
[53] Singh K, Menke H, Andrew M, Lin Q, Rau C, Blunt MJ, et al. Dynamics of snap-off and pore-filling events during two-phase fluid flow in permeable media. Sci Rep 2017:7. https://doi.org/10.1038/s41598-017-05204-4.
[54] Singh K, Jung M, Brinkmann M, Seemann R. Capillary-Dominated Fluid Displacement in Porous Media. Annu Rev Fluid Mech 2019;51:429–49. https://doi.org/10.1146/annurev-fluid-010518.
[55] Singh K, Bultreys T, Raeini AQ, Shams M, Blunt MJ. New type of pore-snap-off and displacement correlations in imbibition. J Colloid Interface Sci 2022;609:384–92. https://doi.org/10.1016/j.jcis.2021.11.109.
[56] Blunt MJ, Bijeljic B, Dong H, Gharbi O, Iglauer S, Mostaghimi P, et al. Pore-scale imaging and modelling. Advances in Water Resources 2013;51:197–216. https://doi.org/10.1016/j.advwatres.2012.03.003.
[57] Thomson PR, Aituar-Zhakupova A, Hier-Majumder S. Image segmentation and analysis of pore network geometry in two natural sandstones. Front Earth Sci (Lausanne) 2018:6. https://doi.org/10.3389/feart.2018.00058.
[58] Shams M, Singh K, Bijeljic B, Blunt MJ. Direct numerical simulation of pore-scale trapping events during capillary-dominated two-phase flow in porous media. Transp Porous Media 2021;138:443–58. https://doi.org/10.1007/s11242-021-01619-w.
[59] Tanino Y, Blunt MJ. Capillary trapping in sandstones and carbonates: Dependence on pore structure. Water Resour Res 2012;48:W08525. https://doi.org/10.1029/2011WR011712.